Soto, J.I., and Hudec, M.R., 2023, Mud volcanoes guided by thrusting in compressional settings: Geology, https://doi.org/10.1130/G51235.1

# Supplemental Material

*Supplemental Material for:*

# Mud Volcanoes Guided by Thrusting in Compressional Settings

**Juan I. Soto[1,2] and Michael R. Hudec[3]**

*[1]Bureau of Economic Geology, Jackson School of Geosciences, The University of Texas at Austin, P.O. Box X, Austin, TX 78713-8924, USA.*
*juan.soto@beg.utexas.edu (ORCID No. 0000-0001-5428-5329)*

*[2]On leave of absence from: Departamento de Geodinámica, Universidad de Granada, Avenida de Fuente Nueva s/n, 18071 Granada, Spain*

*[3]Bureau of Economic Geology, Jackson School of Geosciences, The University of Texas at Austin, University Station, Box X, Austin, TX 78713-8924, USA. michael.hudec@beg.utexas.edu*

---

## CONTENTS

## SEISMIC DATASET

We analyzed the evolution of shale structures in the East Breaks fold-and-thrust belt (EB FTB) using the Crystal WATS® 3D seismic dataset from PGS. This is a wide-azimuth survey covering 13,500 km$^2$, acquired in 2006 and reprocessed with reverse-time prestack depth migration in 2019 (Lebit et al., 2018). Inline-crossline spacing is 30 × 30 meters. The survey is zero phase, plotted using the SEG polarity convention such that a downward increase in impedance is displayed as a peak (black). The survey is processed to a depth of 14.6 km. Confidentiality restrictions prevent us from showing the precise location of the seismic cube in the offshore Gulf of Mexico (GOM), although Fig. S1 shows the general position of the East Breaks protraction area in the northern GOM.

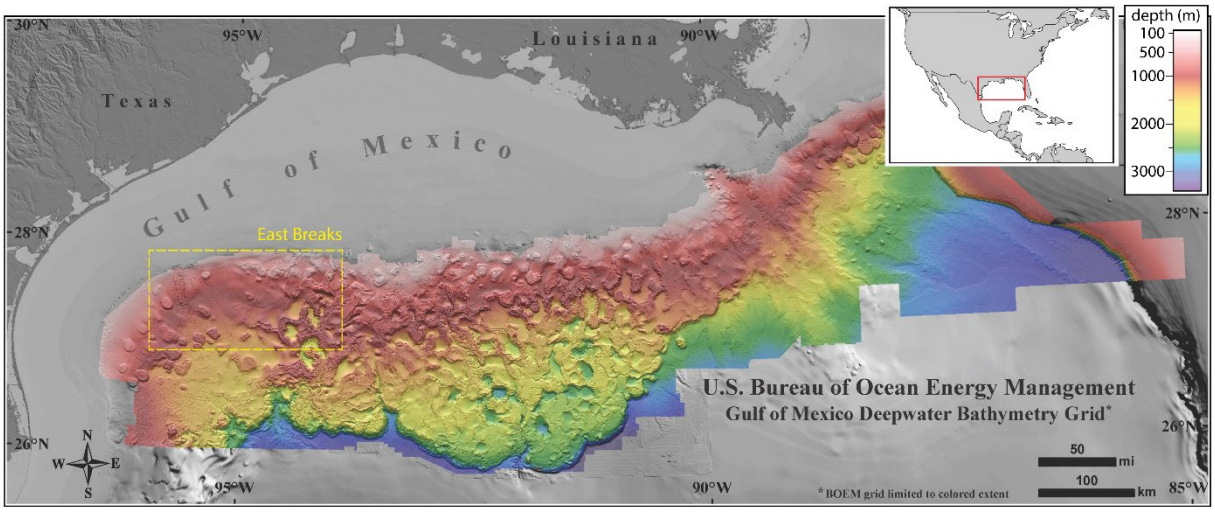


**Figure S1.** Position of the East Breaks protracted area over the bathymetry grid of the deep-water northern Gulf of Mexico (Bjerstedt et al., 2016; BOEM, 2016). The studied seismic cube is situated within the East Breaks. The precise location of the cube cannot be shown due to confidentiality restrictions. Inset shows the geographic position of the map area.

## 3D SEISMIC INTERPRETATION

Horizon interpretations in the seismic cube were oriented to the mobile shales and their roof sequences, as well as to the seismic units situated immediately below. Seismic interpretation was conducted in three dimensions, using DecisionSpace®. Uninterpreted versions of the seismic profiles in Fig. 2 are shown in Fig. S2.

Interpretation of the seismic discontinuities and main reflections was based on palaeontologic information from 19 wells in the study area for which biostratigraphic data are available in multiple publications (e.g., Galloway et al., 2000, 2011; Ewing and Galloway, 2019; Snedden and Galloway, 2019). Of these wells, only four penetrated through the Miocene into Oligocene units (Braithwaite et al., 1988; Dow et al., 1990; Trainor et al., 1990), for example, the Nansen Deep well (cf. Pan, 2002; Nicholson et al., 2012).

According to this information, it is estimated that mobile shales are of Oligocene age (e.g., Camerlo et al., 2004) and that the main unconformity interpreted here is middle Miocene. Shales are detached along a mixed salt–shale detachment, which corresponds to a remanent weld (Fig. 2) of the allochthonous salt in northern GOM (e.g., Hall et al., 1993; Diegel et al., 1995; Peel et al., 1995; Rowan et al., 2004, 2006; Radovich et al., 2007; Hudec et al., 2013). Descriptions of the general structure and seismo-stratigraphy of the area, the structural position and general geometry of the mobile shales, and the configuration of the allochthonous salt are detailed in Hudec et al. (in review). The seismic expression of the mobile-shale structures analyzed in this contribution is documented in Fig. 2, which is accompanied by a larger and uninterpreted version of the seismic profiles and depth slices in Fig. S2.

Two main seismic reflectors have been interpreted systematically in the study area; i.e., a strong positive reflection that describes continuously the fold and thrust structures and the main unconformity (Figs. 2 and S2). The first reflector is considered an early syn-shortening surface of top-Oligocene age (Camerlo et al., 2004), whereas the unconformity occurs within the middle Miocene section. Horizon interpretation was conducted manually over a regularly spaced grid (250 m) formed by in-lines, cross-lines, and arbitrary lines oriented perpendicular to folds. Horizon was then auto-tracked in DecisionSpace®.

Seismic interpretation in 3D has been complemented with surface gridding using the least squares method and a biharmonic smoothing algorithm (with flex passing of 4.0, smoothing modulus of 0.5, and a search radius of 250 m). The resulting gridded surface for the pre-kinematic surface is shown in Figs. 2A and S2A.

Structure filtering (Marfurt et al., 1998; Fehmers and Höcker, 2003; Chopra and Marfurt, 2007; Hale, 2009) and discontinuity filtering (Sobel filter; Bahorich and Farmer, 1995; Marfurt et al., 1998) were also applied for us to inspect the detailed geometry and characteristics of the feeder

systems of shale sheets and the geometry and characteristics of the fractures associated with the thrusts (Fig. S2G). The characteristics of both filters were 2 lines and 15 samples for a structure filter preserving faults, and 2 cross-lines, 3 in-lines, and 15 samples for the Sobel filter.

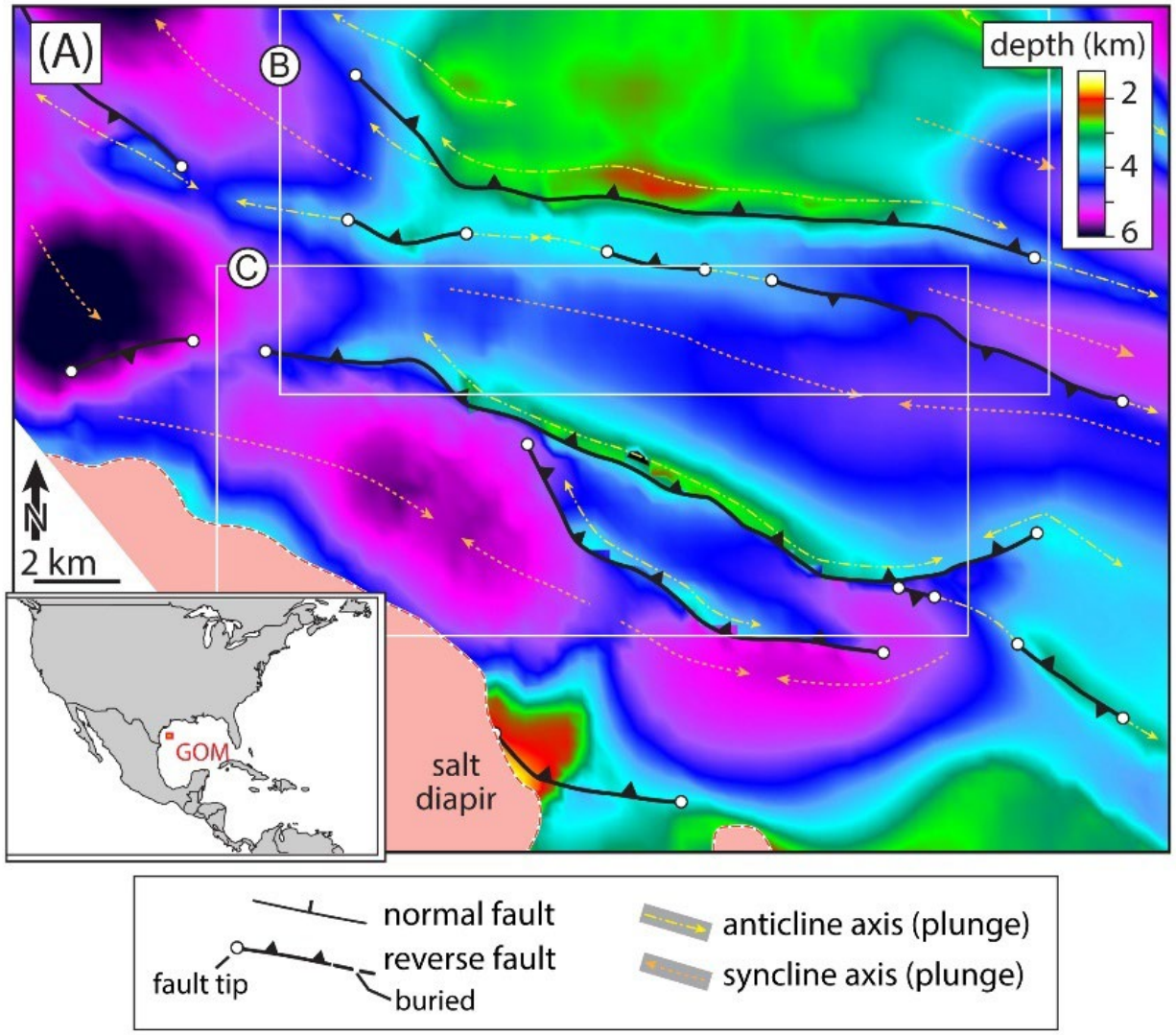


**Figure S2.** (Legend in p. 9).

## UNINTERPRETED VERSION OF SEISMIC PROFILES

The uninterpreted version of the seismic profiles shown in Fig. 2 is included here with a larger size and a simplified geometry of mobile shales. It is also provided various complementary seismic profiles to show the lateral evolution of the fold and thrust structures, as well as of the mud volcanoes, shale sheets, and their associated feeder systems (Figs. S2D to S2L).

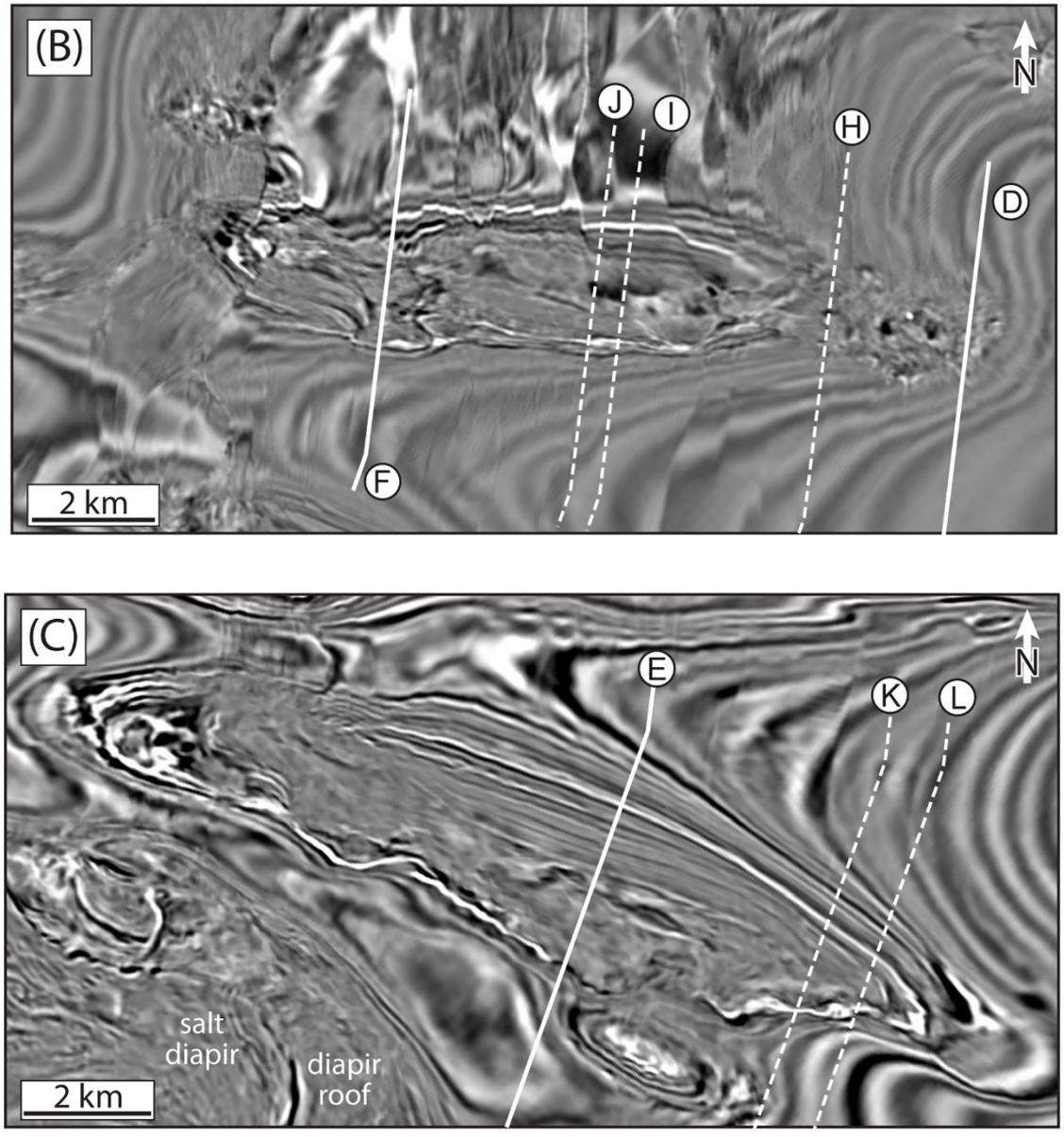


**Figure S2.** (Legend in p. 10).

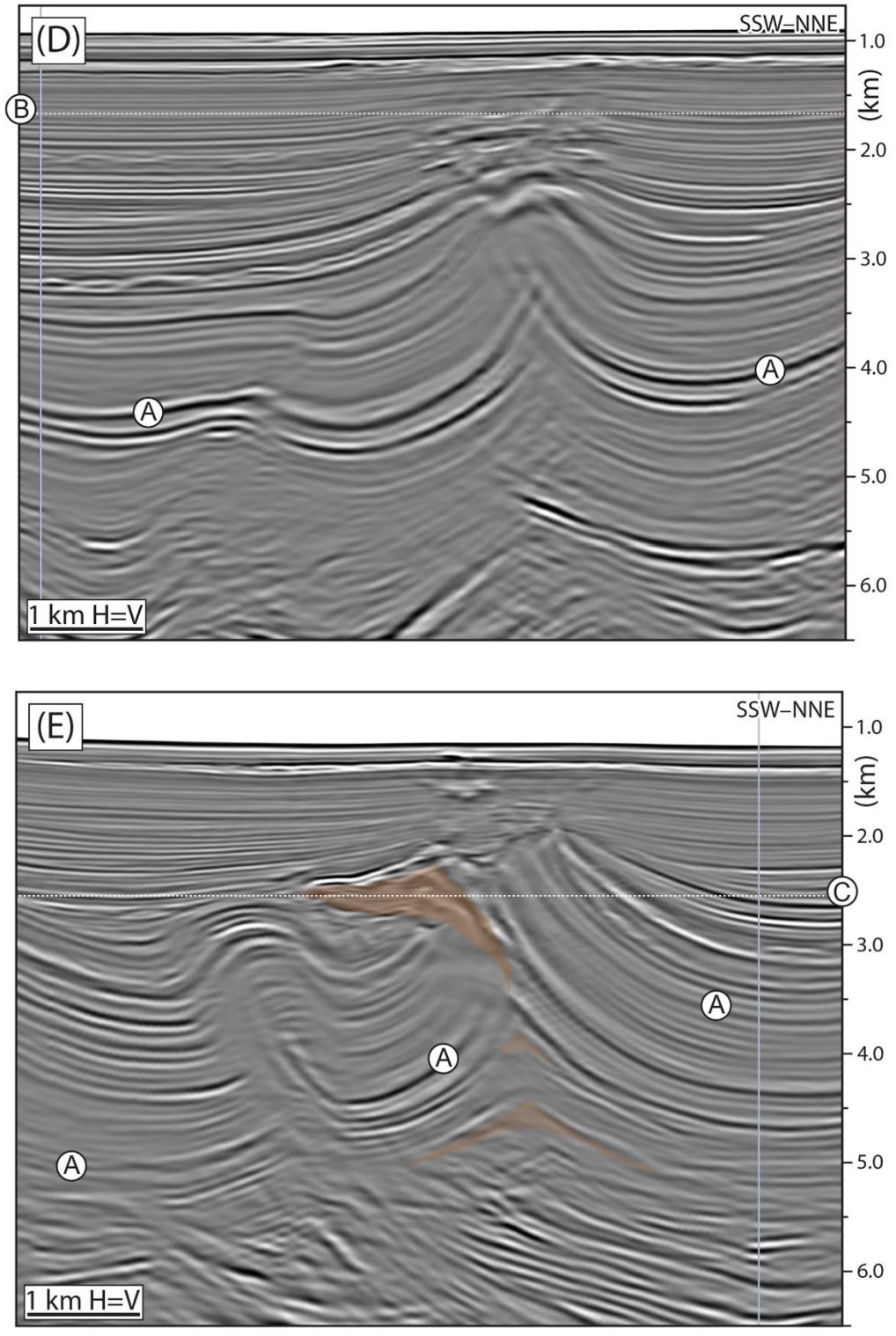


**Figure S2.** (Legend in p. 10).

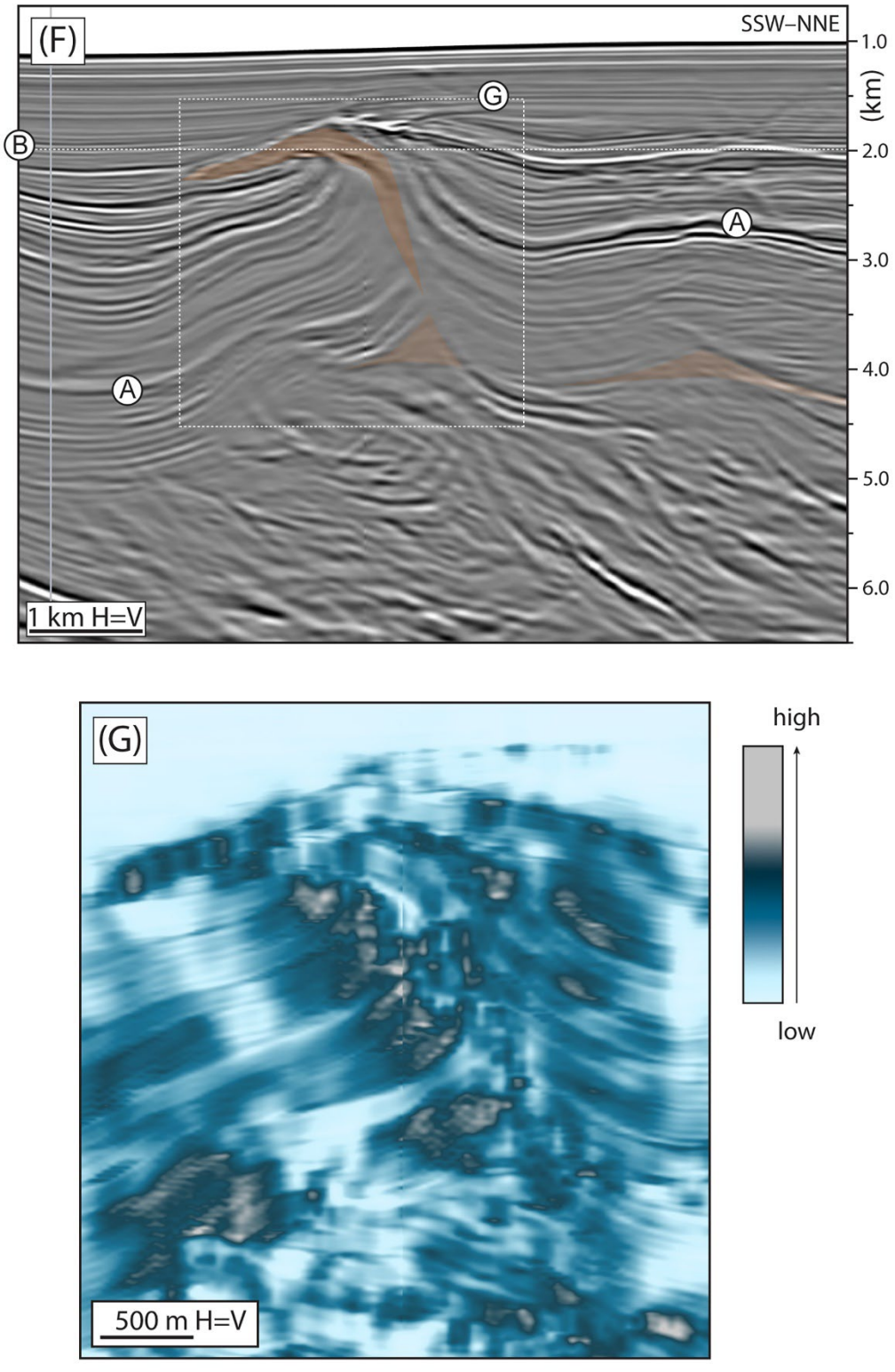


**Figure S2.** (Legend in p. 10).

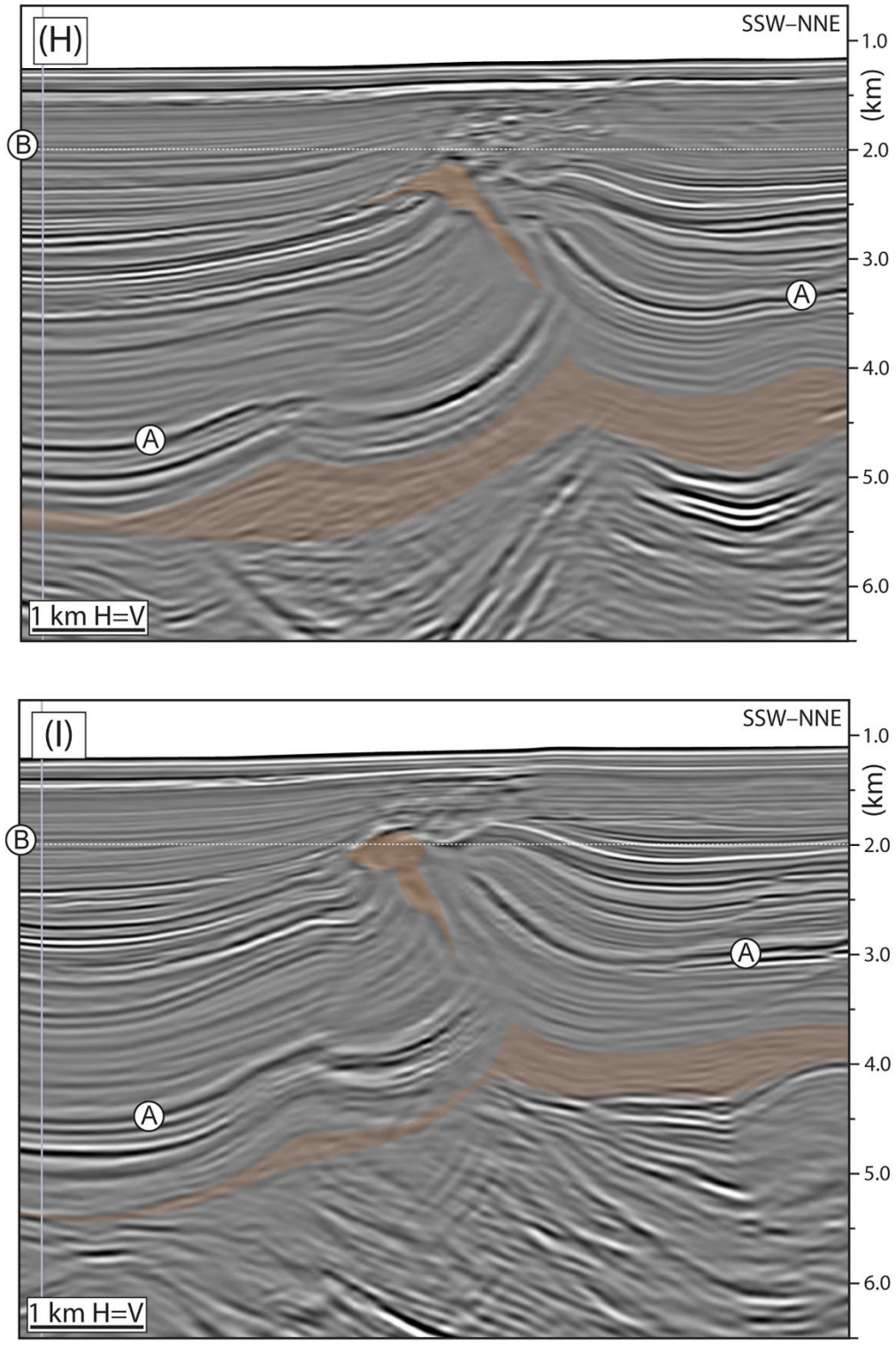


**Figure S2.** (Legend in p. 10).

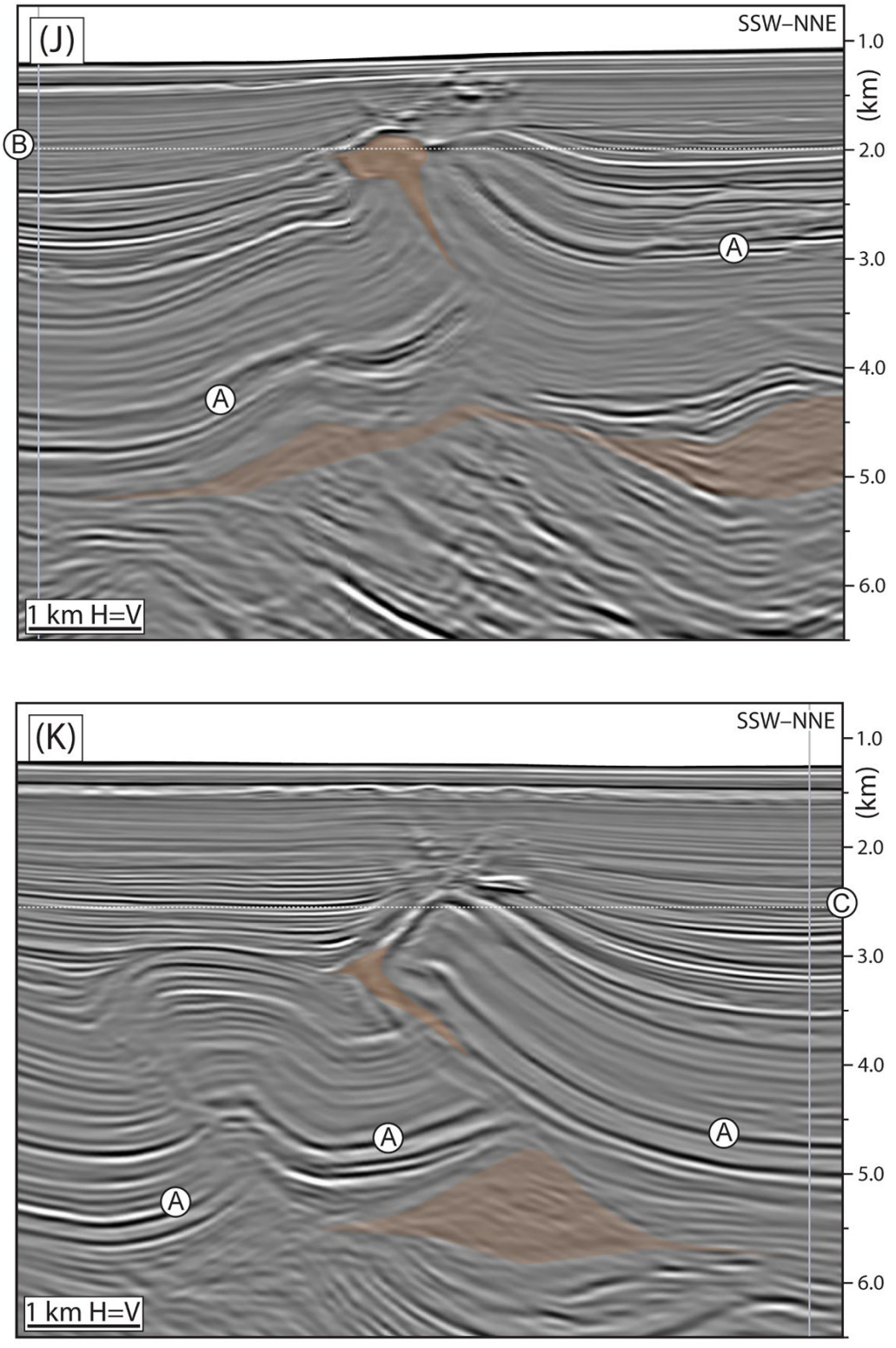


**Figure S2.** (Legend in p. 10).

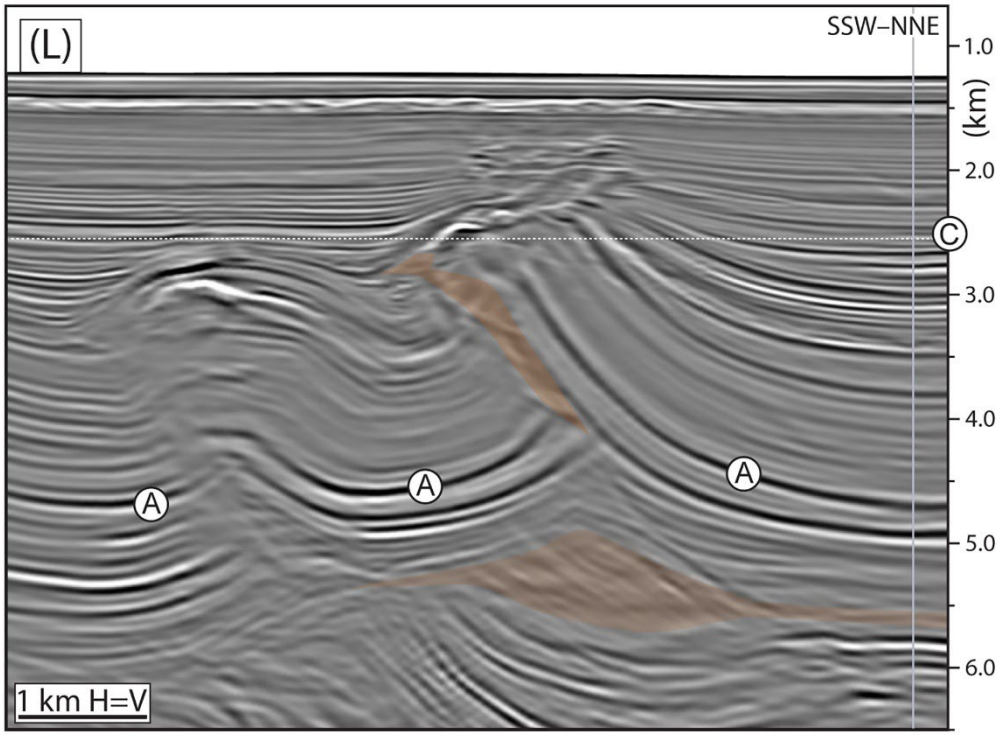


**Figure S2.** Uninterpreted detailed seismic expression of mobile shales in EB FTB (offshore NW Gulf of Mexico), documenting the main structures related to shale sheets. This figure accompanies the interpreted version shown in Fig. 2B trough 2G, including new seismic examples (H) to (L) Seismic examples (B to L) include a simplified interpretation of the mobile shale structures. (A) Structural depth map of a seismic horizon within the syn-shortening sequence in the study area (with a correlated age near the top-Oligocene). This gridded surface corresponds to the seismic reflector marked with an encircled letter A in (D) to (L). Inset shows the general geographic position of the study area within the Gulf of Mexico (GOM) (see Fig. S1). (B) Uninterpreted depth slice at 1990 m. (C) Uninterpreted depth slice at 2500 m. (D) Seismic profile situated near the lateral tip of the fold structure showing the internal geometry of a detachment anticline with zig-zag thrusts at the core and a stack of "inflated shale cores." (E) and (F) Seismic profiles across the central domain of the fold structures shown in (C) and (B), respectively, documenting the occurrence of thrust-related shale sheets. (G) Discontinuity-filter display of the fault zone associated with the thrust in (D). (H) to (J) Seismic profiles documenting different geometries of the extrusive mud-volcano edifices and how they are connected to thrust-related feeder channels. (K) and (L) Seismic profiles showing an incipient shale sheet and how the fluid-migration pathways occur along the thrust surface, which is formed by a network of anastomosing fault fractures. All the seismic profiles are arbitrary lines taken perpendicular to the structural trend of the fold and thrust structures. Encircled letters show the position of the different panels and seismic sections.

## SHORTENING ESTIMATE OF THE FOLD AND THRUST STRUCTURES

Two structures (Figs. 2B and C) were studied through multiple depth slices and along parallel (SSW–NNE) arbitrary seismic lines that are oriented perpendicular to the fold axis (Figs. 2D–F). Fold axis is subhorizontal in most of the WNW–ESE-trending structure (Figs. 2A and S2A), although the fold axis is gently dipping (<2–3°) in the two periclinal closures of the folds. In consequence, the studied arbitrary seismic lines constitute true fold profiles (*sensu* Ramsay, 1967).

In the arbitrary lines we analyzed in detail the following geometric elements for the two key seismic reflectors; i.e., the early syn-shortening surface of late Oligocene age and the unconformity of middle Miocene age: (1) original length ($L_0$); (2) final length ($L_f$); (3) dip angle of the main thrust ($\theta_i$); (4) fault heave ($h$); and (5) horizontal length or advance of the shale sheet ($sh$). These parameters are shown schematically in Fig. S3. Shortening magnitude is calculated through two expressions (e.g, Dahlstrom, 1969; Sánchez-Borrego et al., 2016):

$$S = L_0 - L_f \qquad [1]$$

and

$$\%S = 100 \times \frac{L_0 - L_f}{L_0} \qquad [2],$$

where $L_0$ is the sum of the different segments of the folded surface (Fig. S3). Our shortening estimate is therefore assuming that bed length and layer thickness remain constant during deformation. This assumption is common in structural restorations, although we are thus ignoring possible deformation-related changes, due for example to dissolution, pore reduction, shale flow, and horizontal compaction during shortening (see Fig. 1; e.g., Butler and Paton, 2010; Groshong et al., 2012; Eichelberger et al., 2015; Totake et al., 2018; Wu et al., 2020). In consequence, the values we estimated represent a minimum value of the shortening magnitude.

Shortening was measured in every anticline structure through arbitrary lines spaced every 0.5 km and using the pin lines defined by the hinge points of the two nearby synclines or where the seismic horizon becomes horizontal (Fig. S3) (similarly to Higgins et al., 2009; Totake et al., 2018). $L_f$ corresponds, therefore, to the horizontal distance measured in the fold profile between the vertical axial surfaces of those synclines. The frontal syncline is marked with a dotted, pinned vertical line in the seismic profiles (Figs. S2D–F). Where another fold or thrust structure occurs within these

lines, the pin lines were placed to avoid those secondary structures, to restrict the shortening estimate to the central fold structure that includes the shale sheet (e.g., Fig. S1F). Where the fold crest is eroded, the length of the folded pre-shortening surface was measured along the unconformity. In consequence, the shortening magnitude in those regions is a minimum value of the real total shortening (e.g., Schlische et al., 2014; Totake et al., 2018).

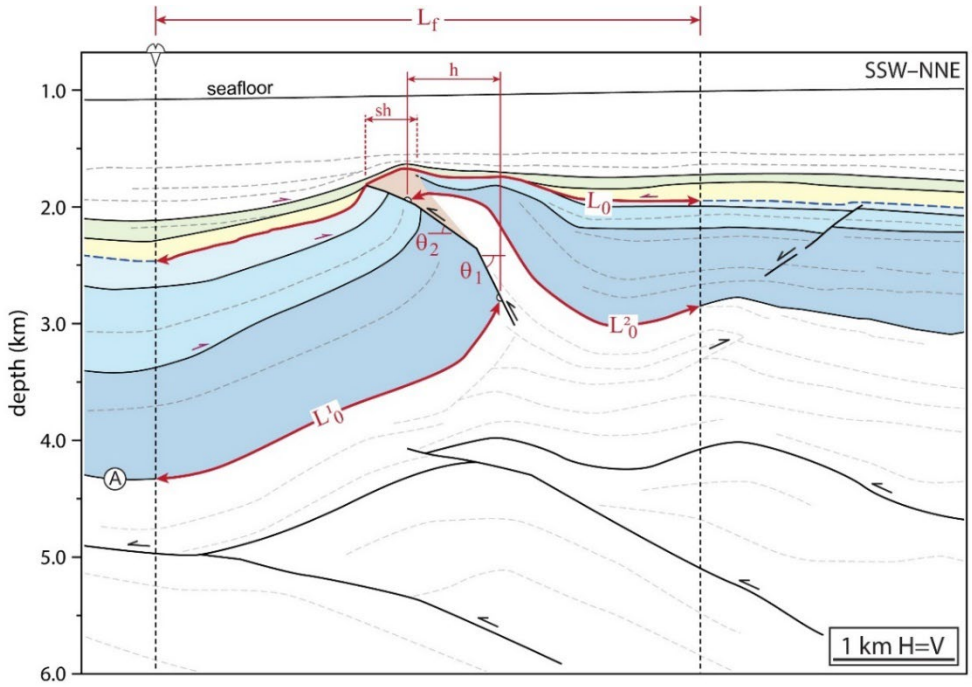


**Figure A3.** Diagram of an arbitrary line showing the main structural elements measured in a fold profile, which were used to estimate the shortening magnitude [equations (1) and (2)] for the two main seismic reflectors (Fig. 2). Initial and original length ($L_0$), final length ($L_f$), dip variations along the thrust surface ($\theta_i$), fault heave ($h$; measured according to the horizontal displacement of the gridded top-Oligocene surface shown in Figs. 2A and S2A), and horizontal advance of the shale sheet ($sh$). Other symbols are shown in Fig. 2.

Measured fold parameters and the associated shortening magnitudes are shown in Tables S1 and S2. The error of the different variables is as follows: (1) shortening uncertainty is considered to be 10% in the pre-shortening surface and 20% for the unconformity; (2) the variation of the dip angle of the thrust is expressed as the average value of the different fault segments, resulting usually in differences of about ±5-7°; and (3) for the fault heave ($h$) and length of the shale sheets, error is ±100 or ±50 m for values ≥ 1 and < 1 km, respectively. All these estimates are represented in a diagram using the distance along fold strike (Bergen and Shaw, 2010) (Figs. 3 and S4).

Correlation between the horizontal advance of the shale sheets with the average dip of the thrust surfaces is shown in Fig. S5.

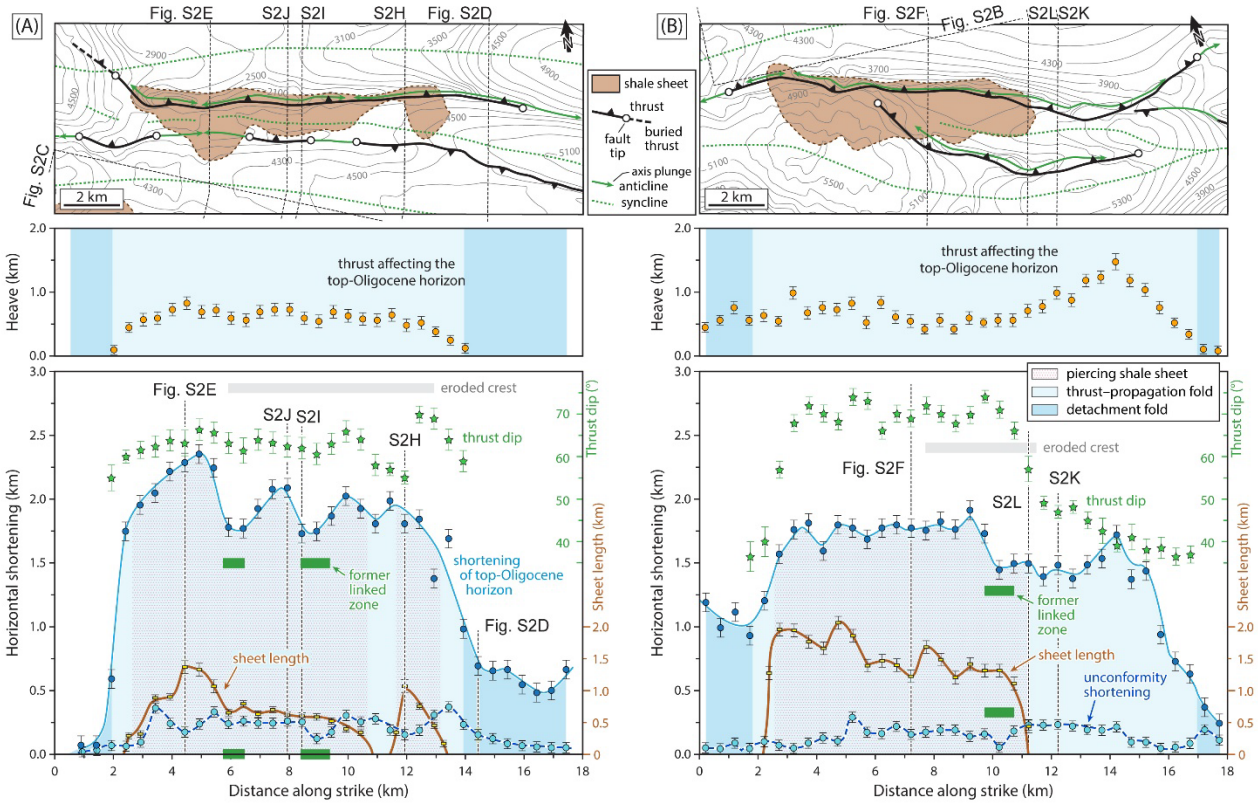


**Figure A4.** Detailed plots for the fold structures analyzed in this study, completing the information shown in Fig. 3. It is documented how the different fold parameters, folding type, shortening magnitude, and shale sheets vary along fold strike. (A) and (B) Diagrams corresponding to the fold structure shown in Figs. 2B and 2C, respectively. Upper panels are depth-contour maps of the early syn-shortening (top-Oligocene) horizon (contour interval is 200 m; Figs. 2A and S2A) and include the distribution of the shale sheets. Intermediate panels show the heave of the thrusts according to the displacement of the Oligocene surface. Lower plots indicate the variation along strike of the shortening magnitude, thrust dip, and horizontal shale-sheet advance. Shortening is estimated according to equation (1) for the top-Oligocene and the unconformity surfaces (Tables S1 and S2). Horizontal scale is measured parallel to the fold strike, using regularly spaced fold profiles (every 0.5 km); it shows the position of the different seismic profiles and depth sections shown in Figs. 2 and S2. Positions of the domains interpreted as former linked zones are marked with a green bar (e.g., Bergen and Shaw, 2010; Totake et al., 2018).

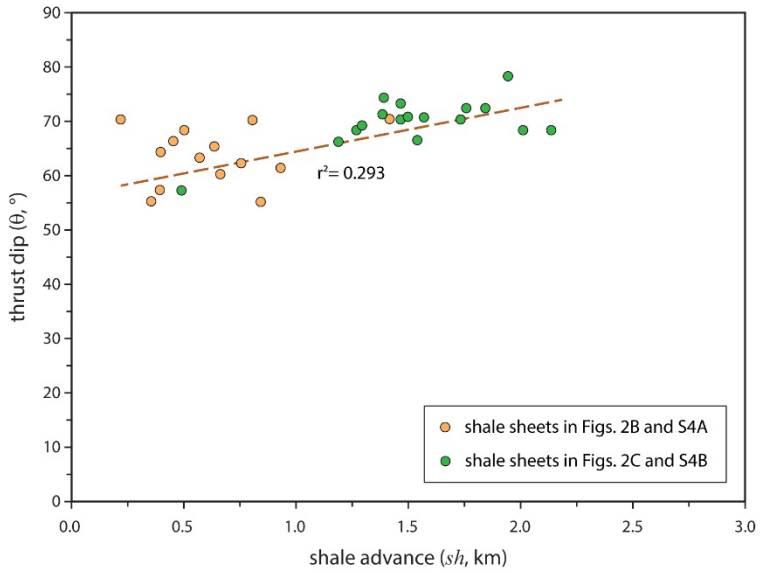


**Figure S5.** Plot showing the relationship between the horizontal advance of the shale sheets and the average dip of the thrust surface. The best correlation between these parameters for the complete dataset is linear and it is included its regression coefficient ($r^2$).

| distance (km) | Fold Structure in Figs. S2B, D, F, and H to J (Shortening, in km and S) | | | | | | | | | | | | shale sheet advance (sh, m) |
|---|---|---|---|---|---|---|---|---|---|---|---|---|---|
| | Lf | Early syn-shortening surface (top Oligocene) | | | | | | | Unconformity (Middle Miocene) | | | | |
| | | fault dip ($\theta_i$) | | fault heave (h) | Lo | S | %S | structure | Lo | S | %S | structure | |
| 0.0 | 3.60 | | | | 4.27 | 0.67 | 15.70 | fold | 3.65 | 0.06 | 1.59 | eroded fold | |
| 0.5 | 3.44 | | | | 3.94 | 0.50 | 12.66 | fold | 3.50 | 0.06 | 1.58 | eroded fold | |
| 1.0 | 3.40 | | | | 3.88 | 0.48 | 12.44 | fold | 3.46 | 0.06 | 1.81 | eroded fold | |
| 1.5 | 3.39 | | | | 3.94 | 0.55 | 13.90 | fold | 3.46 | 0.07 | 1.97 | eroded fold | |
| 2.0 | 3.30 | | | | 3.96 | 0.67 | 16.80 | fold | 3.38 | 0.08 | 2.50 | eroded fold | |
| 2.5 | 3.05 | | | | 3.70 | 0.65 | 17.65 | fold | 3.17 | 0.12 | 3.85 | eroded fold | |
| **3 (Fig. 2D)** | 3.11 | | | | 3.81 | 0.69 | 18.22 | fold | 3.27 | 0.15 | 4.67 | eroded fold & onlaps | |
| 3.5 | 3.09 | 59 | | 131.4 | 4.07 | 0.98 | 24.04 | thrust fold | 3.33 | 0.23 | 7.05 | eroded fold & onlaps | |
| 4.0 | 2.91 | 70 | 65 | 249.9 | 4.60 | 1.69 | 36.66 | thrust fold | 3.28 | 0.37 | 11.27 | eroded fold & onlaps | 219 |
| 4.5 | 3.06 | 68 | 78 | 393.0 | 4.44 | 1.37 | 31.00 | zz thrust fold | 3.37 | 0.31 | 9.30 | eroded fold & onlaps | 498 |
| 5.0 | 2.95 | 70 | 78 | 525.6 | 4.79 | 1.84 | 38.36 | zz thrust fold | 3.14 | 0.19 | 5.92 | pierced fold & onlaps | 806 |
| **5.5 (Fig. S2H)** | 5.44 | 44 | 53 | 495.3 | 7.24 | 1.80 | 24.92 | thrust fold | 5.59 | 0.15 | 2.77 | pierced fold & onlaps | 1120 |
| 6.0 | 5.75 | 57 | | 643.5 | 7.73 | 1.98 | 25.61 | thrust fold | 5.95 | 0.19 | 3.26 | pierced fold & onlaps | 393 |
| 6.5 | 5.78 | 58 | 46 | 574.7 | 7.58 | 1.80 | 23.78 | thrust fold | 6.06 | 0.28 | 4.66 | pierced fold & onlaps | |
| 7.0 | 5.24 | 64 | 45 | 594.4 | 7.16 | 1.92 | 26.83 | zz thrust fold | 5.49 | 0.25 | 4.54 | pierced fold & onlaps | 394 |
| 7.5 | 5.30 | 66 | 48 | 638.6 | 7.32 | 2.02 | 27.62 | zz thrust fold | 5.64 | 0.34 | 6.04 | pierced fold & onlaps | 449 |
| 8.0 | 5.02 | 63 | 52 | 697.6 | 6.88 | 1.86 | 27.08 | zz thrust fold | 5.20 | 0.18 | 3.41 | pierced fold & onlaps | 570 |
| 8.5 | 5.92 | 65 | 57 | 549.2 | 7.67 | 1.75 | 22.78 | zz thrust fold | 6.08 | 0.15 | 2.54 | pierced fold & onlaps | 635 |
| **9 (Fig. S2I)** | 5.07 | 46 | 63 | 590.2 | 6.80 | 1.73 | 25.40 | zz thrust fold | 5.34 | 0.27 | 5.01 | pierced fold & onlaps | 646 |
| **9.5 (Fig. S2J)** | 4.84 | 60 | 50 | 736.1 | 6.92 | 2.08 | 30.10 | zz thrust fold & SZ | 5.10 | 0.27 | 5.20 | pierced fold & onlaps | 658 |
| 10.0 | 4.76 | 62 | 55 | 736.9 | 6.84 | 2.07 | 30.29 | zz thrust fold & SZ | 5.01 | 0.24 | 4.84 | pierced fold & onlaps | 752 |
| 10.5 | 4.40 | 30 | 65 | 702.3 | 6.32 | 1.92 | 30.44 | zz thrust fold & SZ | 4.64 | 0.25 | 5.31 | pierced fold & onlaps | 683 |
| 11.0 | 4.68 | 55 | 63 | 569.8 | 6.44 | 1.77 | 27.44 | zz thrust fold & SZ | 4.94 | 0.26 | 5.26 | pierced fold & onlaps | 840 |
| 11.5 | 4.35 | 42 | 66 | 594.4 | 6.12 | 1.78 | 28.99 | zz thrust fold & SZ | 4.59 | 0.25 | 5.34 | pierced fold & onlaps | 695 |
| 12.0 | 4.16 | 33 | 65 | 727.0 | 6.39 | 2.24 | 34.99 | zz thrust fold & SZ | 4.49 | 0.33 | 7.39 | pierced fold | 1115 |
| 12.5 | 4.06 | 36 | 62 | 692.0 | 6.41 | 2.35 | 36.65 | zz thrust fold & SZ | 4.30 | 0.24 | 5.54 | pierced fold | 1375 |
| **13 (Fig. 2F)** | 4.18 | 70 | 62 | 835.1 | 6.46 | 2.28 | 35.33 | zz thrust fold & SZ | 4.36 | 0.18 | 4.08 | pierced fold | 1415 |
| 13.5 | 3.66 | 32 | 60 | 736.9 | 5.87 | 2.21 | 37.66 | zz thrust fold & SZ | 3.90 | 0.24 | 6.24 | pierced fold & onlaps | 948 |
| 14.0 | 4.08 | 61 | 70 | 604.0 | 6.12 | 2.04 | 33.38 | zz thrust fold | 4.44 | 0.36 | 8.18 | pierced fold & onlaps | 928 |
| 14.5 | 3.93 | 42 | 63 | 574.7 | 5.88 | 1.95 | 33.14 | zz thrust fold | 4.03 | 0.10 | 2.44 | eroded fold | 372 |
| 15.0 | 3.86 | 60 | 75 | 445.7 | 5.61 | 1.74 | 31.12 | zz thrust fold | 3.93 | 0.07 | 1.78 | eroded fold | |
| 15.5 | 1.52 | 55 | | 101.9 | 2.13 | 0.61 | 28.66 | zz thrust fold | 1.59 | 0.08 | 4.73 | fold | 353 |
| 16.0 | 1.48 | | | | 1.54 | 0.06 | 3.83 | fold | 1.52 | 0.04 | 2.77 | fold | |
| 16.5 | 1.69 | | | | 1.75 | 0.06 | 3.35 | fold | 1.71 | 0.02 | 1.14 | very open fold | |

***Notes:***

– *Distance:* measured parallel to fold strike (in km). It is highlighted the cases shown in Figs. 2D and 1F, and in the Supplementary Material (Fig. S2).

– *Abbreviations:* Lo (initial, original length, in km), Lf (final, deformed length, in km), S (shortening, in km), %S (shortening, in %)

– *Description of the structure:* fold (detachment anticline), thrust fold (TA: thrust-related fold and FPF: fault-propagation fold), zz (zig-zag thrust), sz (shear-zone related to the thrust fault, normally close to the upper tip of the fault), frontal backthrust (BT), eroded fold (eroded crest of the anticline), onlaps (onlap geometries developed the late, syn-tectonic sequences lying above the main unconformity; e.g., Fig. 2F), pierced fold (mobile shales piercing the unconformity; e.g., Fig. 2F), and pinched-off (pinched-off anticline with a sub-vertical shale weld and a popup geometry).

– *Fault dip ($\theta_i$):* average angle (in °) of the thrust surface; angles are measured in the lower, intermediate, and upper part of the thrust, respectively.

– *Fault heave (h):* horizontal fault displacement (in m) measured for the Oligocene surface.

– *Dimensions of the shale sheets (sh):* horizontal distance (in m) between the upper tip of the thrust and the frontal front of the allochthonous shale sheet. So, it corresponds to the horizontal advance of the shale sheet over the thrust footwall.

– *Shortening (S and %S):* calculated according to equations (1) and (2). Shortening magnitude is only measured for the central fold structure and does not include other associated structures like frontal backthrusts or forethrusts (e.g., from 2.0 to 3.5 km; Fig. 2F).

**Table S1.** Fold parameters and associated shortening estimate across the fold structure depicted in Figs. S2B, S2D, S2F, and S2H to S2J. Results are represented in Fig. 2A.

S

| distance (km) | Fold Structure in Figs. S2C, E, K, and L (Shortening, in km and %) | | | | | | | | | | | | | shale sheet advance (sh, m) |
|---|---|---|---|---|---|---|---|---|---|---|---|---|---|---|
| | Lf | Early syn-shortening surface (top Oligocene) | | | | | | | | Unconformity (Middle Miocene) | | | | |
| | | fault dip ($\theta_i$) | | | fault heave (h) | Lo | S | %S | structure | Lo | S | %S | structure | |
| 0.0 | 3.69 | 50 | unclear | | 90.3 | 3.93 | 0.24 | 6.11 | thrust fold (TA) | 3.80 | 0.11 | 2.77 | fault-propagation fold (FPF) | |
| 0.5 | 3.82 | 52 | unclear | | 113.0 | 4.19 | 0.37 | 8.83 | TA | 4.00 | 0.18 | 4.52 | FPF | |
| 1.0 | 3.39 | 37.0 | | | 348.7 | 4.02 | 0.63 | 15.58 | TA | 3.47 | 0.07 | 2.14 | FPF | |
| 1.5 | 3.55 | 36.5 | | | 531.1 | 4.28 | 0.73 | 17.07 | TA | 3.60 | 0.05 | 1.49 | FPF | |
| 2.0 | 3.89 | 38.5 | | | 770.6 | 4.82 | 0.94 | 19.41 | TA & backthrust (BT) | 3.93 | 0.04 | 0.99 | FPF | |
| 2.5 | 3.92 | 38 | 42 | | 1051.8 | 5.36 | 1.44 | 26.79 | TA & BT | 4.02 | 0.09 | 2.26 | FPF | |
| 3.0 | 4.92 | 41 | 53 | | 1194.0 | 6.11 | 1.19 | 19.42 | TA & BT | 5.01 | 0.09 | 1.82 | FPF | |
| 3.5 | 5.39 | 39 | 58 | | 1473.6 | 7.10 | 1.72 | 24.15 | zz TA | 5.60 | 0.21 | 3.76 | FPF | |
| 4.0 | 5.11 | 42.5 | | | 1233.0 | 6.62 | 1.51 | 22.82 | TA | 5.29 | 0.18 | 3.48 | FPF | |
| 4.5 | 4.88 | 46 | 62 | | 1195.4 | 6.37 | 1.49 | 23.32 | sz TA | 5.07 | 0.19 | 3.76 | eroded FPF | |
| 5.0 | 4.75 | 48 | | | 884.7 | 6.00 | 1.26 | 20.93 | sz TA | 4.97 | 0.22 | 4.43 | eroded FPF | |
| **5.5 (Fig. S2K)** | 4.24 | 47 | 56 | | 996.4 | 5.86 | 1.61 | 27.54 | sz TA | 4.47 | 0.23 | 5.16 | eroded FPF | |
| 6.0 | 4.27 | 49 | 56 | | 787.3 | 5.69 | 1.42 | 24.96 | sz, zz TA | 4.49 | 0.22 | 4.93 | eroded FPF | 427 |
| **6.5 (Fig. S2L)** | 4.25 | 57 | | 44 | 723.3 | 5.74 | 1.49 | 26.01 | sz, zz TA | 4.48 | 0.23 | 5.04 | eroded FPF | 486 |
| 7.0 | 4.24 | 66 | | 46 | 560.0 | 5.73 | 1.49 | 25.98 | sz, zz TA | 4.42 | 0.18 | 4.18 | eroded FPF | 1189 |
| 7.5 | 4.19 | 71 | | 37 | 565.4 | 5.63 | 1.44 | 25.58 | sz, zz TA | 4.36 | | 4.00 | eroded FPF | 1385 |
| 8.0 | 4.19 | 74 | | 41 | 525.6 | 5.92 | 1.73 | 29.20 | sz, zz TA | 4.35 | 0.16 | 3.60 | eroded FPF | 1385 |
| 8.5 | 4.61 | 70 | | 37 | 604.2 | 6.52 | 1.91 | 29.33 | sz, zz TA | 4.74 | 0.13 | 2.82 | eroded FPF | 1483 |
| 9.0 | 4.15 | 68 | | 41 | 422.5 | 5.91 | 1.76 | 29.80 | sz, zz TA | 4.34 | 0.18 | 4.27 | eroded FPF | 1267 |
| 9.5 | 4.06 | 70 | | 29 | 566.2 | 5.88 | 1.83 | 31.02 | sz, zz TA | 4.24 | 0.18 | 4.36 | eroded FPF, erosion | 1562 |
| 10.0 | 3.82 | 72 | | 40 | 434.2 | 5.57 | 1.75 | 31.43 | sz, zz TA | 3.99 | 0.17 | 4.24 | eroded FPF, erosion | 1755 |
| **10.5 (Fig. 2E)** | 3.86 | 69 | | 37 | 550.2 | 5.63 | 1.77 | 31.48 | sz, zz TA | 4.01 | 0.15 | 3.79 | eroded FPF, erosion | 1292 |
| 11.0 | 3.80 | 70 | | 31 | 619.0 | 5.59 | 1.79 | 32.07 | sz, zz TA | 4.01 | 0.21 | 5.35 | eroded FPF, erosion | 1464 |
| 11.5 | 5.75 | 66 | | 40 | 849.8 | 7.52 | 1.77 | 23.55 | sz, zz TA, fold crest | 5.91 | 0.16 | 2.66 | eroded FPF, erosion | 1535 |
| 12.0 | 5.64 | 73 | | 39 | 534.7 | 7.33 | 1.68 | 22.95 | sz, zz TA, fold crest | 5.82 | 0.18 | 3.08 | eroded FPF, erosion | 1464 |
| 12.5 | 5.47 | 78 | | 26 | 835.8 | 7.24 | 1.77 | 24.49 | sz, zz TA, fold crest | 5.89 | 0.42 | 7.20 | eroded FPF, erosion | 1940 |
| 13.0 | 5.07 | 68 | | 18 | 738.9 | 6.87 | 1.80 | 26.17 | sz, zz TA, fold crest | 5.17 | 0.10 | 1.88 | eroded FPF, erosion | 2132 |
| 13.5 | 4.97 | 70 | | 25 | 772.6 | 6.56 | 1.60 | 24.31 | sz, zz TA, fold crest | 5.09 | 0.12 | 2.41 | pierced FPF | 1729 |
| 14.0 | 4.82 | 72 | | 20 | 681.6 | 6.76 | 1.94 | 28.72 | sz, zz TA, fold crest | 4.90 | 0.08 | 1.59 | pierced FPF | 1842 |
| 14.5 | 4.49 | 68 | | 25 | 997.2 | 6.38 | 1.89 | 29.62 | sz, zz TA, fold crest | 4.53 | 0.04 | 0.96 | eroded FPF | 2008 |
| 15.0 | 4.74 | 70 | | 19 | 564.9 | 6.31 | 1.58 | 24.96 | sz, zz TA, fold crest | 4.80 | 0.07 | 1.37 | eroded, open FPF | |
| 15.5 | 4.28 | 40 | | | 644.1 | 5.48 | 1.19 | 21.80 | zz, pinched-off | 4.38 | 0.10 | 2.27 | eroded, open FPF | 2304 |
| 16.0 | 3.92 | 46 | | | 560.4 | 4.81 | 0.89 | 18.57 | zz, pinched-off | 3.96 | 0.04 | 1.07 | eroded, open FPF | 2520 |
| 16.5 | 3.85 | 47 | 53 | | 769.4 | 5.10 | 1.25 | 24.45 | zz, duplex. pinched-off | 3.93 | 0.08 | 1.98 | open fold | 2491 |
| 17.0 | 3.22 | 47 | | | 571.7 | 4.07 | 0.85 | 20.89 | zz, duplex. pinched-off | 3.26 | 0.04 | 1.08 | open fold | 2687 |
| 17.5 | 3.25 | 25 | | | 460.8 | 4.77 | 1.52 | 31.85 | zz, duplex. pinched-off | 3.29 | 0.04 | 1.29 | open fold | 2122 |

***Notes:***

– *Distance:* measured parallel to fold strike (in km). It is highlighted the cases shown in Fig. 2E and in the Supplementary Material (Fig. S2).
– *Abbreviations:* Lo (initial, original length, in km), Lf (final, deformed length, in km), S (shortening, in km), %S (shortening, in %)
– *Description of the structure:* fold (detachment anticline), thrust fold (TA: thrust-related fold and FPF: fault-propagation fold), zz (zig-zag thrust), sz (shear-zone related to the thrust fault, normally close to the upper tip of the fault), frontal backthrust (BT), eroded fold (eroded crest of the anticline), onlap (onlap geometries developed the late, syn-tectonic sequences lying above the main unconformity; e.g., Fig. 2F), pierced fold (mobile shales piercing the unconformity; e.g., Fig. 2F), and pinched-off (pinched-off anticline with a sub-vertical shale weld and a popup geometry).
– *Fault dip ( $\theta_i$ ):* average angle (in °) of the thrust surface; angles are measured in the lower, intermediate, and upper part of the thrust, respectively
– *Fault heave (h):* horizontal fault displacement (in m) measured for the Oligocene surface.
– *Dimensions of the shale sheets (sh):* horizontal distance (in m) between the upper tip of the thrust and the frontal front of the allochthonous shale sheet. So, it corresponds to the horizontal advance of the shale sheet over the thrust footwall.
– *Shortening (S and %S):* calculated according to equations (1) and (2). Shortening magnitude is only measured for the central fold structure and does not include other associated structures like frontal backthrusts or forethrusts (e.g., from 2.0 to 3.5 km; Fig. 2F).

**Table S2.** Fold parameters and associated shortening estimate across the fold structure depicted in Figs. S2C, S2E, S2K, and S2L. Results are represented in Fig. 2B.

## REFERENCES CITED

Bahorich, M., and Farmer, S., 1995, 3-D seismic discontinuity for faults and stratigraphic features: the coherence cube: The Leading Edge, v. 14, p. 1053–1098, doi:10.1190/1.1437077.

Bergen, K.J., and Shaw, J.H., 2010, Displacement profiles and displacement-length scaling relationships of thrust faults constrained by seismic-reflection data: AAPG Bulletin, v. 122, p. 1209–1219, doi:10.1130/B26373.1.

Bjerstedt, T.W., Kramer, K., and Shedd, W.W., 2016, New bathymetry grid of the deepwater Gulf of Mexico: Poster presented at Gordon Research Conference (Natural Gas Hydrate Systems), Galveston, Texas, 28 February–4 March, doi:10.13140/RG.2.2.26286.61762.

BOEM (Bureau of Ocean Energy Management), 2016, Northern GoM deepwater bathymetry grid from 3D seismic: https://www.boem.gov/oil-gas-energy/mapping-and-data/map-gallery/northern-gom-deepwater-bathymetry-grid-3d-seismic (accessed December 2022).

Braithwaite, P., Armentrout, J.M., Beeman, C.E., and Malecek, S.J., 1988, East Breaks Block 160 field, offshore, Texas: a model for deep water deposition of sand: presented at Offshore Technology Conference, Houston, 2–5 May, Paper OTC-5696-MS, doi:10.4043/5696-MS.

Butler, R.W.H., and Paton, D.A., 2010, Evaluating lateral compaction in deepwater fold and thrust belts: how much are we missing from "nature's sandbox": GSA Today, v. 20, p. 4–10, doi:10.1130/GSATG77A.1.

Camerlo, R., Meyer, D., and Meltz, R., 2004, Shale tectonism in the northern Port Isabel Fold Belt, *in* Post, P.J., Olson, D.L., Lyons, K.T., Palmes, S.L., Harrison, P.F., and Rosen, N.C., eds., Salt-sediment Interactions and Hydrocarbon Prospectivity: Concepts, Applications and Case Studies for the 21st. Century: Houston, 24th Annual Gulf Coast Section SEPM Foundation, Bob F. Perkins Research Conference, p. 817–839.

Chopra, S., and Marfurt, K.J., 2007, Volumetric curvature attributes add value to 3D seismic data interpretation: The Leading Edge, v. 26, p. 856–867, doi:10.1190/1.2756864.

Dahlstrom, C.D.A., 1969, The upper detachment in concentric folding: Bulletin of Canadian Petroleum Geology, v. 17, p. 326–346, doi:10.35767/gscpgbull.17.3.326.

Diegel, F.A., Karlo, J.F., Schuster, D.C., Shoup, R.C., and Tauvers, P.R., 1995, Cenozoic structural evolution and tectonostratigraphic framework of the northern Gulf Coast continental margin, *in* Jackson, M.P.A., Roberts, D.G., and Snelson, S., eds., Salt Tectonics: A Global Perspective: AAPG Memoir, v. 65, p. 109–151.

Dow, W.G., Yukler, M.A., Senftle, J.T., Kennicuttii, M.C., and Armentrout, J.M., 1990, Miocene oil source beds in the East Breaks Basin, Flex-Trend, Offshore, Texas, *in* Schumacher, D., and Perkins, B.F., eds., Gulf Coast Oils and Gases: Their Characteristics, Origin, Distribution, and Exploration and Production Significance: Proceedings of the Annual Research Conference, Gulf Coast Section, Society of Economic Paleontologists and Mineralogists Foundation, v. 9, p. 139–150, doi:10.5724/gcs.90.09.0139.

Eichelberger, N.W., Hughes, A.N., and Nunns, A.G., 2015, Combining multiple quantitative structural analysis techniques to create robust structural interpretations: Interpretation, v. 3, p. SAA89–SAA104, doi:10.1190/INT-2015-0016.1.

Ewing, T.E., and Galloway, W.E., 2019, Evolution of the Northern Gulf of Mexico Sedimentary Basin, *in* Miall, A.D., ed., The Sedimentary Basins of the United States and Canada (2nd. Edition): Amsterdam, Elsevier, p. 627–694, doi:10.1016/B978-0-444-63895-3.00016-4.

Fehmers, G.C., and Höcker, C., 2003, Fast structural interpretation with structure-oriented filtering: Geophysics, v. 68, p. 1286–1293, doi:10.1190/1.1598121.

Galloway, W.E., Ganey-Curry, P.E., Li, X., and Buffler, R.T., 2000, Cenozoic depositional history of the Gulf of Mexico basin: AAPG Bulletin, v. 84, p. 1743–1774, doi:10.1306/8626C37F-173B-11D7-8645000102C1865D.

Galloway, W.E., Whiteaker, T.L., and Ganey-Curry, P.E., 2011, History of Cenozoic North American drainage basin evolution, sediment yield, and accumulation in the Gulf of Mexico basin: Geosphere, v. 7, p. 938–973, doi:10.1130/GES00647.1.

Groshong, R.H., Withjack, M.O., Schlische, R.W., and Hidayah, T.N., 2012, Bed length does not remain constant during deformation: recognition and why it matters: Journal of Structural Geology, v. 41, p. 86–97, doi:10.1016/j.jsg.2012.02.009.

Hale, D., 2009, Structure-oriented smoothing and semblance: Boulder, Colorado, Colorado School of Mines, Center for Wave Phenomena, Publ. CWP-635, p. 1–10.

Hall, D.J., Bowen, B.E., Rosen, R.N., Wu, S., and Bally, A.W., 1993, Mesozoic and early Cenozoic development of the Texas margin: a new integrated cross-section from the Cretaceous shelf edge to the Perdido Fold Belt, *in* Pindell, J.L., and Perkins, B.F., eds., Mesozoic and Early Cenozoic Development of the Gulf of Mexico and Caribbean Region–A Context for Hydrocarbon Exploration: SEPM Society for Sedimentary Geology, v. 13, p. 21–31, doi:10.5724/gcs.92.13.0021.

Higgins, S., Clarke, B., Davies, R.J., and Cartwright, J., 2009, Internal geometry and growth history of a thrust-related anticline in a deep water fold belt: Journal of Structural Geology, v. 31, p. 1597–1611, doi:10.1016/j.jsg.2009.07.006.

Hudec, M.R., Jackson, M.P.A., and Peel, F.J., 2013, Influence of deep Louann structure on the evolution of the northern Gulf of Mexico: AAPG Bulletin, v. 97, p. 1711–1735, doi:10.1306/04011312074.

Hudec, M.R., Peel, F.J., Soto, J.I., and Apps, G., under review, Interaction between salt and mobile shale in the East Breaks fold belt, northwestern Gulf of Mexico: Marine and Petroleum Geology.

Lebit, H.D., Clavaud, M., Whitehead, S., Opdyke, S.N., and Luneburg, C., 2018, The Port Isabel Fold Belt: Neogene gravitational spreading in the East Breaks, Western Gulf of Mexico: AAPG Annual Convention and Exhibition, Salt Lake City, Utah, Search and Discovery Article #90323.

Marfurt, K.J., Kirlin, R.L., Farmer, S.L., and Bahorich, M.S., 1998, 3-D seismic attributes using a semblance-based coherency algorithm: Geophysics, v. 63, p. 1150–1165, doi:10.1190/1.1444415.

Nicholson, A.J., Wilkins, S., Contrino, Ch., Termina, J., Hertz, M., and Dembicki, H., 2012, Fault and top seal strength at Nansen Field, East Breaks, Gulf of Mexico: AAPG Annual Convention and Exhibition, Long Beach, California, Search and Discovery Article #90142.

Pan, J.G.S., 2002, The Nansen Discovery, East Breaks Block 602, deepwater Gulf of Mexico—a geophysicist's perspective: SEG Annual Meeting, Salt Lake City, Utah, Paper SEG-2002-0428.

Peel, F.J., Travis, C.J., and Hossack, J.R., 1995, Genetic structural provinces and salt tectonics of the Cenozoic offshore U.S. Gulf of Mexico: A preliminary analysis, *in* Jackson, M.P.A., Roberts, D.G., and Snelson, S., eds., Salt Tectonics: A Global Perspective: AAPG Memoir, v. 65, p. 153–175.

Radovich, B.J., Connors, C.D., and Moon, J., 2007, Deep imaging of the Paleogene, Miocene structure and stratigraphy of the Western Gulf of Mexico using 2D pre-stack depth migration of mega-regional onshore to deep water, long-offset seismic data, *in* Kennan, L., Pindell, J., and Rosen, N.C., eds., The Paleogene of the Gulf of Mexico and Caribbean Basins: Processes, Events, and Petroleum Systems: 27th Annual Gulf Coast Section SEPM Foundation, Bob F. Perkins Research Conference, p. 307–323.

Ramsay, J.G., 1967, Folding and Fracturing of Rocks: New York, McGraw-Hill, 568 p.

Rowan, M.G., Peel, F.J., and Vendeville, B.C., 2004, Gravity-driven fold belts on passive margins, *in* McClay, K.R., ed., Thrust Tectonics and Hydrocarbon Systems: AAPG Memoir, v. 82, p. 157–182.

Rowan, M., Inman, K.F., and Fiduk, J.C., 2006, Oligocene-Miocene extension at the Louann level in the Northern Gulf of Mexico: Kinematic models and examples: Gulf Coast Association of Geological Societies Transactions, v. 55, p. 725–732.

Sánchez-Borrego, I.R., Soto, J.I., Rueda, M., and Santos Betancor, I., 2016, Nonparametric estimation to reconstruct the deformation history of an active fold in the Caspian Basin: Mathematical Geosciences, v. 48, p. 985–1011, doi:10.1007/s11004-016-9650-1.

Schlische, R.W., Groshong, R.H., Withjack, M.O., and Hidayah, T.N., 2014, Quantifying the geometry, displacements, and subresolution deformation in thrust-ramp anticlines with growth and erosion: from models to seismic-reflection profile: Journal of Structural Geology, v. 69, p. 304–319, doi:10.1016/j.jsg.2014.07.012.

Snedden, J.W., and Galloway, W.E., 2019, The Gulf of Mexico Sedimentary Basin: Depositional Evolution and Petroleum Applications: Cambridge, Cambridge University Press, 326 p.

Totake, Y., Butler, R.W.H., Bond, C.E., and Aziz, A., 2018, Analyzing structural variations along strike in a deep-water thrust belt: Journal of Structural Geology, v. 108, p. 213–229, doi:10.1016/j.jsg.2017.06.007.

Trainor, D.M., Williams, D.F., and Armentrout, J., 1990, Isotope chronostratigraphy: High-resolution stratigraphic correlation of exploration wells within the South Galveston and East Breaks areas, Gulf of Mexico: AAPG Annual Convention, San Francisco, California, Search and Discovery Article #91003.

Wu, J., McClay, K., and de Vera, J., 2020, Growth of triangle zone fold-thrusts within the NW Borneo deep-water fold belt, offshore Sabah, southern South China Sea: Geosphere, v. 16, p. 329–356, doi:10.1130/GES02106.1.